International Journal of Solids and Structures 267 (2023) 112148

Contents lists available at ScienceDirect

International Journal of Solids and Structures

journal homepage: www.elsevier.com/locate/ijsolstr

Finite strain elastoplastic bulging of circular diaphragms

Khurram Suleman, Federico Bosi *

Department of Mechanical Engineering, University College London, Torrington Place, WC1E 7JE, London, UK

ARTICLE INFO

Dataset link: https://github.com/fbosi/ElastoplasticDiaphragmBulging

Keywords:
Membranes
Inflatable structures
Bulge test
Thin films
Elastoplasticity

ABSTRACT

The inflation of planar thin films represents a phenomenon widely employed by engineering and biological systems, with applications ranging from pressure sensors and material characterization to growing skins in the human body. In this paper, the bulging of plane circular membranes composed of isotropic elastoplastic materials is analytically, computationally and experimentally studied. An analytical finite strain formulation is developed and implemented to model the deformation response of inflated thin films. The solution accurately predicts the elastic and plastic phases of bilinear and nonlinear elastoplastic materials, for both small and large plastic strains. It shows that a sudden change in the full-field strain distribution during diaphragm inflation is associated with the plastic strain localization that first develops at the membrane apex. The results are compared with finite element simulations for a wide range of material parameters, showing an excellent agreement. The mathematical formulation is also validated by bulge tests performed on ETFE membranes, representative of a bilinear elastoplastic response, and aluminium foils that show a nonlinear plastic behaviour. The comparison between theoretical predictions and experimental measures proves the validity of the proposed model at small and large plastic strains, which promises to find applications in the modelling of the finite strain inflation of thin films, especially for the determination of elastoplastic material parameters through bulge testing.

1. Introduction

Structural membranes find growing use in a vast number of applications due to their wide range of intrinsic optical, thermal and mechanical properties (McCrum et al., 1997). They can be synthesized with materials that span from polymers (Strong, 2006) to metals (Diehl et al., 2008) in various combinations of features that encompass transparency, resistance to UV (Yadav and Chiu, 2019), extreme temperatures and large deformations. Their application in pneumatic systems ranges from inflatable cushions of mega-structures (Koch, 2004) to micromechanical systems, including shape morphing devices (Siéfert et al., 2020; Jin et al., 2020), actuators for soft robotics (Shepherd et al., 2011; Li et al., 2014), pressure sensors (Melzer et al., 2015), biological membranes (Rausch and Kuhl, 2014) and balloon catheters for biomedical applications (Inoue et al., 1984).

Due to their lightweight nature, tiny thickness, and ability to undergo large deformations before failure, the mechanical response of inflatable membranes has attracted considerable attention. In particular, the effect of material properties (Benet et al., 2019; Ye et al., 2019), geometric configurations (Emery and Fu, 2021; Needleman, 1976) and imperfection (Wang et al., 2019) on the critical and post-critical behaviour of inflatable thin films has been studied to either prevent structural instabilities or harness their snap-through effects. Additionally, the bulge (also named inflation or diaphragm) test has become one of the most preferred methods to characterize the response of membrane materials because it complements uniaxial tensile tests and offers advantages over planar biaxial experiments (Bosi and Pellegrino, 2017; Machado et al., 2012; Rossi et al., 2022). In particular, the inhomogeneous and biaxial stress state in bulge tests can delay the onset of failure by localized instability, thus enabling to reach higher strain levels compared to uniaxial tests (Galliot and Luchsinger, 2011; Chen, 2020). Furthermore, bulge tests reduce wrinkling, stress concentrations and premature failure observable in the arms of cruciform planar biaxial experiments, enabling access to large strains and multiple stress–strain conditions from a single test (Bosi and Pellegrino, 2018; Chen et al., 2016). Hence, it is of fundamental importance to accurately model the mechanics of bulging diaphragm when subjected to out-of-plane pressure and undergoing large deformations.

Previous works include modelling and experiments on inflatable square (Tinoco et al., 2021), rectangular (Xiang et al., 2005) and circular (Chaudhuri and DasGupta, 2014; Fox and Goulbourne, 2008) thin films. Due to axisymmetric geometry, the most common test remains the inflation of circular planar membranes, which was modelled by several authors with different levels of accuracy and material constitutive behaviour. The seminal work by Hencky (1915) assumed elastic

* Corresponding author.
E-mail address: f.bosi@ucl.ac.uk (F. Bosi).

https://doi.org/10.1016/j.ijsolstr.2023.112148
Received 27 November 2022; Received in revised form 16 January 2023; Accepted 3 February 2023
Available online 14 February 2023

material, constant membrane thickness, small rotations and strains. It was later extended to include pre-stress (Campbell, 1956), incorporate the effect of normal loading in the tangential direction (Fichter, 1997), auxeticity (Lim, 2016) and large rotations (Lian et al., 2016; Yang et al., 2017). A summary of different small strain solutions based on Henky's approach was presented by Coelho et al. (2014).

Finite strain axisymmetric solutions based on an incompressible hyperelastic material (Mooney, 1940; Rivlin, 1948) were developed by Adkins and Rivlin (1952) using the general framework of Love (1927), and by Foster (1967b,a) employing the theory of Green and Zerna (1968). The finite strain inflation of membranes constituted of isotropic rigid plastic material was introduced by Wang and Shammamy (1969) and Hill (1950) by considering Lévy–Mises constitutive relation with a power-law material model. The analysis of the bulging of plastic materials was extended by Rees (1995), Liu et al. (2015), Reis et al. (2016), Chen et al. (2016, 2018) to consider the inflation of circular and elliptical anisotropic thin metal sheets. In the works of Rees (1995) and Chen et al. (2016, 2018), the stresses at the apex of bulged sheets were considered non-equibiaxial and obtained through equilibrium and plastic flow rule by assuming negligible elastic strains, whereas, Liu et al. (2015) and Reis et al. (2016) assumed negligible influence of anisotropy and used equibiaxial stress state at the apex of the membrane. The aforementioned works employ rigid-plastic constitutive models suitable to capture large plastic deformations, but by neglecting the elastic strains they are unable to assess (i) the response at small elastoplastic strains and (ii) the features associated with the onset of plasticity and when elastic and plastic phases coexist in inflated membranes. These pieces of information are fundamental when bulge tests are used to develop constitutive models for elastoplastic materials, or to characterize the response of engineering materials that are implemented in inflatable structures and mechanisms working below the onset of permanent deformations. Hence, despite the quest for more accurate and overarching models that include a large variety of material responses for the inflation of circular membranes, there is still a lack of analytical solutions that include a comprehensive elastoplastic formulation capable of capturing small and large plastic strains, and identifying the onset and development of plastic deformations.

In this work, the analysis of the bulging of isotropic elastoplastic plane circular membranes subjected to uniform pressure is carried out analytically, computationally and experimentally to predict the behaviour of the material when both the elastic and plastic strains are of the same magnitude, but also at large plastic strains. Therefore, the developed model and its open source numerical implementation can be regarded as a generalization of Wang and Shammamy (1969) and Hill (1950) works because it reduces to their models when elastic strains are neglected, but it goes beyond them by considering small and large elastoplastic strains. A detailed finite strain formulation is presented and solved in Section 2. It is followed by a discussion of the results in Section 3, and their validation through finite element analysis. The new formulation is also applied to predict the response of bilinear and nonlinear elastoplastic materials during diaphragm inflation, with experiments carried out on ethylene tetrafluoroethylene (ETFE) and thin aluminium films to validate the developed mathematical model.

2. Finite strain elastoplastic formulation

2.1. Governing equations

A plane circular and isotropic membrane of radius r_0 is subjected to a uniform pressure p, Fig. 1. Ignoring bending and shear stresses, the equilibrium equation in tangential T and vertical z directions can be written in terms of true stresses as (Wang and Shammamy, 1969; Hill, 1950)

$$\frac{\partial}{\partial \xi}(h\xi\sigma_r) = h\sigma_\theta, \tag{1}$$

$$\sigma_r = -\frac{p\xi\left[1+\left(\frac{\partial w}{\partial \xi}\right)^2\right]^{1/2}}{2h\frac{\partial w}{\partial \xi}}, \tag{2}$$

where ξ is the deformed radial coordinate, h is the deformed thickness, σ_r and σ_θ are the principal stresses in tangential and circumferential directions, and w is the vertical displacement, as illustrated in Fig. 1(b). Due to material isotropy and consequent axisymmetric deformation, the equilibrium in the circumferential direction is not considered as the stresses in the θ direction remain unchanged.

The logarithmic strains in the tangential, circumferential and thickness (or normal) directions for an axisymmetric geometry undergoing large displacements are given by (Wang and Shammamy, 1969)

$$\varepsilon_r = \ln\left[\left(1+\frac{\partial u}{\partial r}\right)^2 + \left(\frac{\partial w}{\partial r}\right)^2\right]^{\frac{1}{2}}, \tag{3}$$

$$\varepsilon_\theta = \ln\left(1+\frac{u}{r}\right), \tag{4}$$

$$\varepsilon_h = \ln\left(\frac{h}{h_0}\right), \tag{5}$$

where r is the undeformed radial coordinate, u is the radial displacement and h_0 is the initial thickness of the membrane, Fig. 1(b). The deformed radial coordinate ξ can be expressed as a function of r and u as $\xi = r + u$.

The incremental form of the constitutive equations for an isotropic bilinear elastoplastic material in plane-stress state can be described in each direction as

$$\frac{\partial \varepsilon_r}{\partial t} = \frac{1}{E}\left(\frac{\partial \sigma_r}{\partial t} - \upsilon\frac{\partial \sigma_\theta}{\partial t}\right) + \frac{1}{H\bar{\sigma}}\frac{\partial \bar{\sigma}}{\partial t}\left(\sigma_r - \frac{\sigma_\theta}{2}\right), \tag{6}$$

$$\frac{\partial \varepsilon_\theta}{\partial t} = \frac{1}{E}\left(\frac{\partial \sigma_\theta}{\partial t} - \upsilon\frac{\partial \sigma_r}{\partial t}\right) + \frac{1}{H\bar{\sigma}}\frac{\partial \bar{\sigma}}{\partial t}\left(\sigma_\theta - \frac{\sigma_r}{2}\right), \tag{7}$$

$$\frac{\partial \varepsilon_h}{\partial t} = -\frac{\upsilon}{E}\left(\frac{\partial \sigma_r}{\partial t} + \frac{\partial \sigma_\theta}{\partial t}\right) - \frac{1}{H\bar{\sigma}}\frac{\partial \bar{\sigma}}{\partial t}\left(\frac{\sigma_r + \sigma_\theta}{2}\right), \tag{8}$$

where H is the plastic modulus, related to the elastic E and tangent E_t moduli by $H = \frac{EE_t}{E-E_t}$. The right hand side of Eqs. (6)–(8) contains elastic and plastic strain increments, according to Prandtl-Reuss equations. Eqs. (1)–(8) form a system of governing equations for the finite strain bulging of a plane circular elastoplastic membrane. There are eight unknowns in this system, namely, σ_r, σ_θ, ε_r, ε_θ, ε_h, w, u and h. The Eqs. (1) to (8) are solved simultaneously in the following section, where the undeformed radial coordinate r can be treated as the independent variable.

2.2. Solution

Using the chain rule and the relation $\xi = r + u$, the derivatives with respect to ξ in Eqs. (1) and (2) can be replaced with derivatives with respect to r. Then, employing the strain–displacement relations (3) to (5), Eqs. (1) and (2) take the form

$$r\,e^{\varepsilon_\theta}\frac{\partial \sigma_r}{\partial r} + (\sigma_r - \sigma_\theta)\sqrt{e^{2\varepsilon_r} - \left(\frac{\partial w}{\partial r}\right)^2} + r\,\sigma_r\,e^{\varepsilon_\theta}\frac{\partial \varepsilon_h}{\partial r} = 0 \tag{9}$$

and

$$\frac{\partial w}{\partial r} = -\frac{r\ p\ e^{\varepsilon_r+\varepsilon_\theta-\varepsilon_h}}{2\,h_0\,\sigma_r}, \tag{10}$$

respectively. By eliminating the horizontal displacement u from Eqs. (3) and (4), the compatibility condition can be described as

$$r\frac{\partial \varepsilon_\theta}{\partial r} = e^{\varepsilon_r-\varepsilon_\theta}\sqrt{1-\left(\frac{\partial w}{\partial r}\right)^2 e^{-2\varepsilon_r}} - 1. \tag{11}$$

Substituting the expression of $\frac{\partial w}{\partial r}$ from Eq. (10) into Eqs. (9) and (11) gives

$$r\frac{\partial \varepsilon_\theta}{\partial r} = e^{\varepsilon_r-\varepsilon_\theta}\sqrt{1-\left(\frac{r\,p\,e^{\varepsilon_r+\varepsilon_\theta-\varepsilon_h}}{2\,h_0\,\sigma_r}\right)^2 e^{-2\varepsilon_r}} - 1 \tag{12}$$

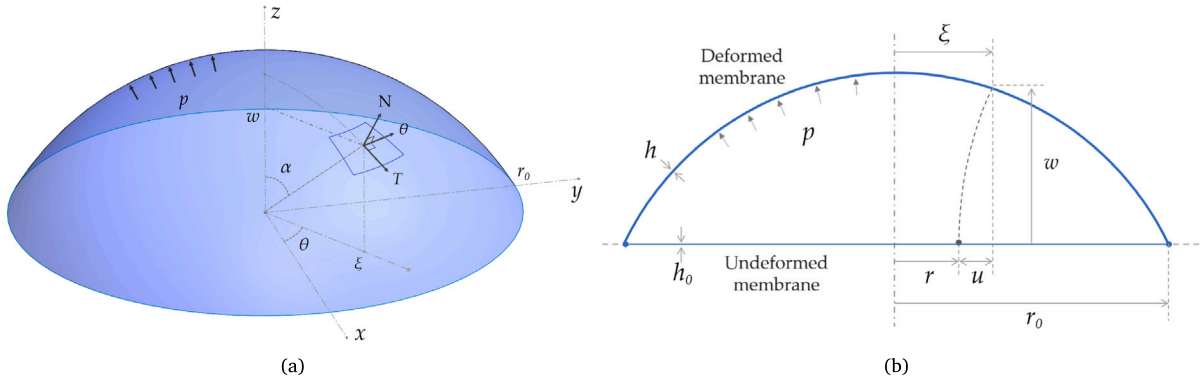

(a) (b)

Fig. 1. (a) Three-dimensional view of the inflated circular membrane showing the different coordinate systems employed in the analysis: cylindrical $\xi\theta z$ and local $NT\theta$. (b) Cross-section of the membrane in the undeformed and deformed configurations.

and

$$r\,e^{\epsilon_\theta}\frac{\partial\sigma_r}{\partial r}+(\sigma_r-\sigma_\theta)\sqrt{e^{2\epsilon_r}-\left(\frac{r\,p\,e^{\epsilon_r+\epsilon_\theta-\epsilon_h}}{2\,h_0\,\sigma_r}\right)^2}+r\,\sigma_r\,e^{\epsilon_\theta}\frac{\partial\epsilon_h}{\partial r}=0. \tag{13}$$

Eqs. (12) and (13) have only stress and strain components as unknowns, and they can be used with the constitutive model and boundary conditions to solve the axisymmetric inflation problem. To utilize the constitutive equations, the stress components σ_r and σ_θ can be parameterized as (Wang and Shammamy, 1969)

$$\sigma_r=\frac{2}{\sqrt{3}}\bar{\sigma}\cos\phi, \tag{14}$$

$$\sigma_\theta=\bar{\sigma}\left(\frac{1}{\sqrt{3}}\cos\phi+\sin\phi\right). \tag{15}$$

The parameterization is introduced to write the unknowns in terms of the von Mises stress $\bar{\sigma}$ and the variable ϕ, which denotes the relative contribution of stress components in the equivalent stress $\bar{\sigma}$:

$$\phi=\arctan\left[\frac{2}{\sqrt{3}}\frac{\sigma_\theta}{\sigma_r}-\frac{1}{\sqrt{3}}\right]. \tag{16}$$

Inserting the expressions for σ_r and σ_θ from Eqs. (14) and (15) in the constitutive relations (6) to (8) gives

$$\begin{aligned}\frac{\partial\epsilon_r}{\partial t}&=\frac{\partial\bar{\sigma}}{\partial t}\left\{\cos\phi\left(\frac{2-\nu}{\sqrt{3}E}+\frac{\sqrt{3}}{2H}\right)-\sin\phi\left(\frac{\nu}{E}+\frac{1}{2H}\right)\right\}\\&+\frac{\partial\phi}{\partial t}\bar{\sigma}\left\{\sin\phi\left(\frac{\nu-2}{\sqrt{3}E}\right)-\cos\phi\frac{\nu}{E}\right\},\end{aligned} \tag{17}$$

$$\begin{aligned}\frac{\partial\epsilon_\theta}{\partial t}&=\frac{\partial\bar{\sigma}}{\partial t}\left\{\sin\phi\left(\frac{1}{E}+\frac{1}{H}\right)+\cos\phi\left(\frac{1-2\nu}{\sqrt{3}E}\right)\right\}\\&+\frac{\partial\phi}{\partial t}\bar{\sigma}\left\{\sin\phi\left(\frac{2\nu-1}{\sqrt{3}E}\right)+\cos\phi\frac{1}{E}\right\},\end{aligned} \tag{18}$$

$$\begin{aligned}\frac{\partial\epsilon_h}{\partial t}&=\frac{\partial\bar{\sigma}}{\partial t}\left\{-\cos\phi\left(\frac{\sqrt{3}\nu}{E}+\frac{\sqrt{3}}{2H}\right)-\sin\phi\left(\frac{\nu}{E}+\frac{1}{2H}\right)\right\}\\&+\frac{\partial\phi}{\partial t}\bar{\sigma}\left\{\sin\phi\frac{\sqrt{3}\nu}{E}-\cos\phi\frac{\nu}{E}\right\}.\end{aligned} \tag{19}$$

Assuming that all the variables are known at the previous state 't', the expression of ϵ_r, ϵ_θ and ϵ_h can be found at the current state '$t+\Delta t$' by integrating Eqs. (17)–(19). As an example, the integration of Eq. (17) gives

$$\begin{aligned}\int_t^{t+\Delta t}\frac{\partial\epsilon_r}{\partial t}dt&=\int_t^{t+\Delta t}\left\{\cos\phi\left(\frac{2-\nu}{\sqrt{3}E}+\frac{\sqrt{3}}{2H}\right)-\sin\phi\left(\frac{\nu}{E}+\frac{1}{2H}\right)\right\}\frac{\partial\bar{\sigma}}{\partial t}dt\\&+\int_t^{t+\Delta t}\bar{\sigma}\left\{\sin\phi\left(\frac{\nu-2}{\sqrt{3}E}\right)-\cos\phi\frac{\nu}{E}\right\}\frac{\partial\phi}{\partial t}dt.\end{aligned} \tag{20}$$

Using the trapezoidal rule, Eq. (20) can be expanded as

$$\begin{aligned}\epsilon_r^{t+\Delta t}&=\epsilon_r^t+\frac{1}{2}\left\{\left(\cos\phi^t+\cos\phi^{t+\Delta t}\right)\left(\frac{2-\nu}{\sqrt{3}E}+\frac{\sqrt{3}}{2H}\right)\right.\\&\left.-\left(\sin\phi^t+\sin\phi^{t+\Delta t}\right)\left(\frac{\nu}{E}+\frac{1}{2H}\right)\right\}\left(\bar{\sigma}^{t+\Delta t}-\bar{\sigma}^t\right)\\&+\frac{1}{2}\left\{\frac{\nu-2}{\sqrt{3}E}\left(\bar{\sigma}^t\sin\phi^t+\bar{\sigma}^{t+\Delta t}\sin\phi^{t+\Delta t}\right)\right.\\&\left.-\frac{\nu}{E}\left(\bar{\sigma}^t\cos\phi^t+\bar{\sigma}^{t+\Delta t}\cos\phi^{t+\Delta t}\right)\right\}\left(\phi^{t+\Delta t}-\phi^t\right).\end{aligned} \tag{21}$$

Similarly, Eqs. (18) and (19) can be integrated to obtain the expression of ϵ_θ and ϵ_h at the current time step $t+\Delta t$. Substituting σ_r and σ_θ from Eqs. (14) and (15) into Eqs. (12) and (13), and writing them for the current time step gives

$$r\frac{\partial\epsilon_\theta^{t+\Delta t}}{\partial r}=e^{\epsilon_r^{t+\Delta t}-\epsilon_\theta^{t+\Delta t}}\sqrt{1-\left(\frac{\sqrt{3}\,r\,p^{t+\Delta t}\,e^{\epsilon_r^{t+\Delta t}+\epsilon_\theta^{t+\Delta t}-\epsilon_h^{t+\Delta t}}}{4\,h_0\,\bar{\sigma}^{t+\Delta t}\,\cos\phi^{t+\Delta t}}\right)^2e^{-2\epsilon_r^{t+\Delta t}}}-1 \tag{22}$$

and

$$\begin{aligned}&r\,e^{\epsilon_\theta^{t+\Delta t}}\frac{2}{\sqrt{3}}\left(\frac{\partial\bar{\sigma}^{t+\Delta t}}{\partial r}\cos\phi^{t+\Delta t}-\bar{\sigma}^{t+\Delta t}\sin\phi^{t+\Delta t}\frac{\partial\phi^{t+\Delta t}}{\partial r}\right)\\&+\bar{\sigma}^{t+\Delta t}\left(\frac{1}{\sqrt{3}}\cos\phi^{t+\Delta t}-\sin\phi^{t+\Delta t}\right)\\&\times\sqrt{e^{2\epsilon_r^{t+\Delta t}}-\left(\frac{\sqrt{3}\,r\,p^{t+\Delta t}\,e^{\epsilon_r^{t+\Delta t}+\epsilon_\theta^{t+\Delta t}-\epsilon_h^{t+\Delta t}}}{4\,h_0\,\bar{\sigma}^{t+\Delta t}\,\cos\phi^{t+\Delta t}}\right)^2}\\&+r\frac{2}{\sqrt{3}}\bar{\sigma}^{t+\Delta t}\cos\phi^{t+\Delta t}\,e^{\epsilon_\theta^{t+\Delta t}}\frac{\partial\epsilon_h^{t+\Delta t}}{\partial r}=0.\end{aligned} \tag{23}$$

The strain components at the current time step, $\epsilon_r^{t+\Delta t}$, $\epsilon_\theta^{t+\Delta t}$ and $\epsilon_h^{t+\Delta t}$, found by numerical integration as in Eq. (21), were then substituted in Eqs. (22) and (23). The resultant equations have $\bar{\sigma}^{t+\Delta t}$, $\phi^{t+\Delta t}$ and their derivatives as the unknown variables, forming a system of two differential equations. They were manipulated to obtain an explicit form, where the derivatives of the unknowns appear on one side of the equation and all the algebraic expressions on the other side. The explicit system of equations was then solved numerically through the Euler method, using a general function form

$$\begin{aligned}\bar{\sigma}_{r+\Delta r}^{t+\Delta t}&=\bar{\sigma}_r^{t+\Delta t}+\left[\frac{\partial\bar{\sigma}}{\partial r}\right]_r^{t+\Delta t}\Delta r,\\\phi_{r+\Delta r}^{t+\Delta t}&=\phi_r^{t+\Delta t}+\left[\frac{\partial\phi}{\partial r}\right]_r^{t+\Delta t}\Delta r.\end{aligned} \tag{24}$$

The system of Eqs. (24) represents the discretization of the radial domain at the instant $t+\Delta t$, where Δr is the mesh size. To complete

the solution procedure, initial and boundary conditions are utilized. Only one half of the cross-section in Fig. 1(b) is solved due to symmetry. All the variables are zero in the undeformed state except ϕ, which is determined by writing the complete form of the constitutive equations Eqs. (6)–(8) and solving for the first deformed state in the elastic regime. In this case, time integration is not required and the equations Eqs. (22) to (24) can be written without the time superscripts. The variables found for the first deformed state were then used as initial conditions for the incremental solution. Boundary conditions are required at the centre, $r = 0$, and at the clamped edge, $r = r_0$. At $r = 0$, both stress components are equal, so that Eq. (16) gives the value of ϕ at the apex of the membrane as

$$\phi_0 = \arctan \frac{1}{\sqrt{3}}, \tag{25}$$

which remains the same at any instant of time. The equivalent stress at the centre $\bar{\sigma}_0$ is given as input in the solution procedure. Hence, knowing $\bar{\sigma}_0$ and ϕ_0 at $r = 0$, the derivatives $\left[\frac{\partial \bar{\sigma}}{\partial r}\right]_{r=0}^{t+\Delta t}$ and $\left[\frac{\partial \phi}{\partial r}\right]_{r=0}^{t+\Delta t}$ can be determined to initiate the solution. The pressure load p is treated as unknown, which is guessed initially and corrected by repeating the iterations until the boundary conditions at the outer edge are satisfied. At $r = r_0$, the displacements u and w are zero; hence, Eq. (4) gives null circumferential strain at the outer edge, $\left[\varepsilon_\theta\right]_{r=r_0} = 0$. After acquiring the solution for one time step, $\bar{\sigma}_0$ is incremented for the next time instant, and a new pressure value is found. In this way, all the unknowns are determined as a function of the radial coordinate r for the entire deformation history of the membrane.

3. Results and discussion

The analytical formulation from the previous section was implemented in a Matlab script and run for different material models. The script can be found at github.com/fbosi/ElastoplasticDiaphragmBulging. The proposed model was validated against small and large plastic strains through the comparison with finite element (FE) results for different ratios between elastic and plastic moduli, Section 3.1. Additionally, the experimental validation was conducted in Section 3.2 to prove the applicability of the proposed solution to different classes of materials and its good accuracy when the elastic and plastic strains are of similar magnitude and coexist in the inflated sheet. The mathematical model was experimentally validated through bulge tests performed on ETFE and thin aluminium sheets, representative of bilinear elastoplastic and elasto nonlinear-plastic material responses, respectively.

3.1. Comparison with FEA

This section presents the results of the FE simulations run in Abaqus 2019 (Dassault Systèms) for different values of material parameter E/H, in order to validate the presented solution procedure. The material model was bilinear elastoplastic, characterized by the elastic modulus $E = 2.5$ GPa, plastic modulus H and yield strength $\sigma_y = 150$ MPa. The Poisson's ratio ν was set as 0.35 because it was found to have a negligible effect on the deformation behaviour in comparison to the elastic and plastic moduli (Fichter, 1997). Geometric non-linear analyses were performed, where a quarter of the circular membrane was modelled, thanks to symmetry conditions. The membrane's initial thickness h_0 was set to 100 μm, with the outer radius was $r_0 = 50$ mm. Uniform pressure was applied normal to the surface of the membrane, while the outer boundary was clamped.

The normalized vertical displacement w/r_0 and the radial strain ε_0 at the apex of the membrane are plotted against the dimensionless pressure pr_0/Eh_0 in Figs. 2(a) and 2(b). Both analytical and FE analyses are reported for $E/H = [2, 5, 10, 20, 50, 100]$, in addition to the finite strain elastic solution. There is an excellent agreement between the present solution and FEA as their curves are hardly distinguishable for all values of E/H, throughout the entire range of biaxial strains investigated, which reach up to 50% at the apex of the bulged membrane. Hence, the comparison proves the capability of the model to predict both small and large plastic strains. The small strain elastic solution (Fichter, 1997) has been added in Fig. 2(a) to quantify the error when using small strain formulation, which grows with increasing pressure. It can be noted that the small strain formulation is only accurate up to $pr_0/Eh_0 = 0.05$, when the difference with respect to the large strain solution is 4.9%. After this point, the small strain solution diverges from the finite strain result.

To further compare the current results and FEA throughout the entire membrane, the normalized equivalent stress $\bar{\sigma}/\sigma_y$, vertical displacement w/r_o and the principal strain components ε_r and ε_θ are plotted in Fig. 3 against the undeformed dimensionless radius r/r_0 for $E/H = 10$, taken at five instants close or beyond the onset of plastic deformation. These instants are associated with the deformation states when the maximum equivalent stress at the membrane's apex $\bar{\sigma}_0$ is 0.99, 1.05, 1.1, 1.2 and 1.5 times the yield strength σ_y.

In the plots of Figs. 3(a)–3(d), the lowermost blue curve is before the occurrence of plasticity, with $\bar{\sigma}/\sigma_y < 1$. The four successive curves of Figs. 3(a) and 3(c) show a drastic increase of stress and strain magnitude at the centre ($r/r_0 = 0$) when compared to the values at the outer edge ($r/r_0 = 1$). This is due to the rapid increase in the rate of deformation in the region where plasticity has been reached, which starts from the apex of the membrane. The point of discontinuity that appears as a cusp on the curves of Figs. 3(a) and 3(c) is moving towards the outer edge, denoting the spreading of the plastic region outwards. There is no discontinuity for vertical displacement in Fig. 3(b) because the deformed profile of the membrane remains continuous. The circumferential strain ε_θ also does not show an abrupt change of distribution related to the elastic limit as it remains zero at the boundary, and there is a smooth decrease of magnitude from the apex to the edge, Fig. 3(d).

The results obtained from the analytical formulation are in excellent agreement with FEA for every curve of Figs. 3(a)–3(d), and the tiny difference is only due to the approximate satisfaction of the boundary condition at the edge of the membrane in the analytical method, $\left[\varepsilon_\theta\right]_{r=r_0} \approx 0$. The criterion chosen for convergence in the Matlab script is $\left[\varepsilon_\theta\right]_{r=r_0} \leq \left[\varepsilon_\theta\right]_{r=0}/100$, as below this value the computational time increases significantly.

The distribution of stress, strain and displacement components along the radius of the membrane can be converted into full-field contour plots by mapping the results on the deformed membrane utilizing axisymmetry. The contour plots of normalized equivalent stress $\bar{\sigma}/\sigma_y$ and out-of-plane displacement w/r_o from FE and current results are plotted in Figs. 4(a) and 4(b) for $\bar{\sigma}_0/\sigma_y = 1.1$, which corresponds to the middle curve of Figs. 3(a) and 3(b), when almost two-third of the membrane radial coordinate has undergone plasticity. Additionally, the contours of horizontal strain component ε_{xx} are plotted in Figs. 4(c) and 4(d) for the instants $\bar{\sigma}_0/\sigma_y = 0.99$ and $\bar{\sigma}_0/\sigma_y = 1.05$. They represent the strain fields just before and after the onset of plasticity, showing an abrupt change in strain distribution when plastic deformations occur, with the maximum strain moving from the edge of the diaphragm to the apex. It should be noted that such a sudden change of strain contour, associated with plastic strain localization, would also be observable when plotting the radial strain ε_r, Fig. 3(c), or the vertical strain ε_{yy}, due to material isotropy. The change in strain distribution at the onset of plasticity is attributed to the inhomogeneous strain distribution during bulge tests, coupled with Poisson's effect. Although the sharpness of the strain localization at the onset of permanent deformations, Figs. 3(c) and 4(d), depends on material parameters, it could be used to develop an experimental imaging procedure to determine the elastic limit of thin-film materials through bulge tests, which is part of future works. It can be argued that such sudden change in strain distribution is caused by the difference between the elastic and plastic moduli occurring at a well-defined yield point from the theoretical bilinear model, and therefore it might not be so sharp if the material shows nonlinearities

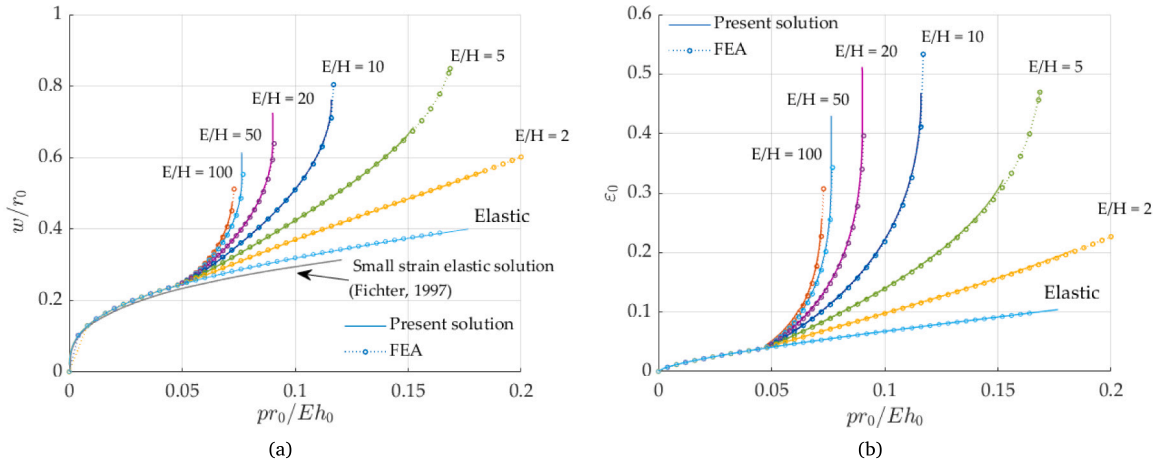

Fig. 2. (a) Normalized vertical displacement w/r_0 and b) radial strain ε_0 at the apex of the inflated membrane plotted against the non-dimensional pressure pr_0/Eh_0 for FE and present solutions for elastic material and when $E/H = [2, 5, 10, 20, 50, 100]$.

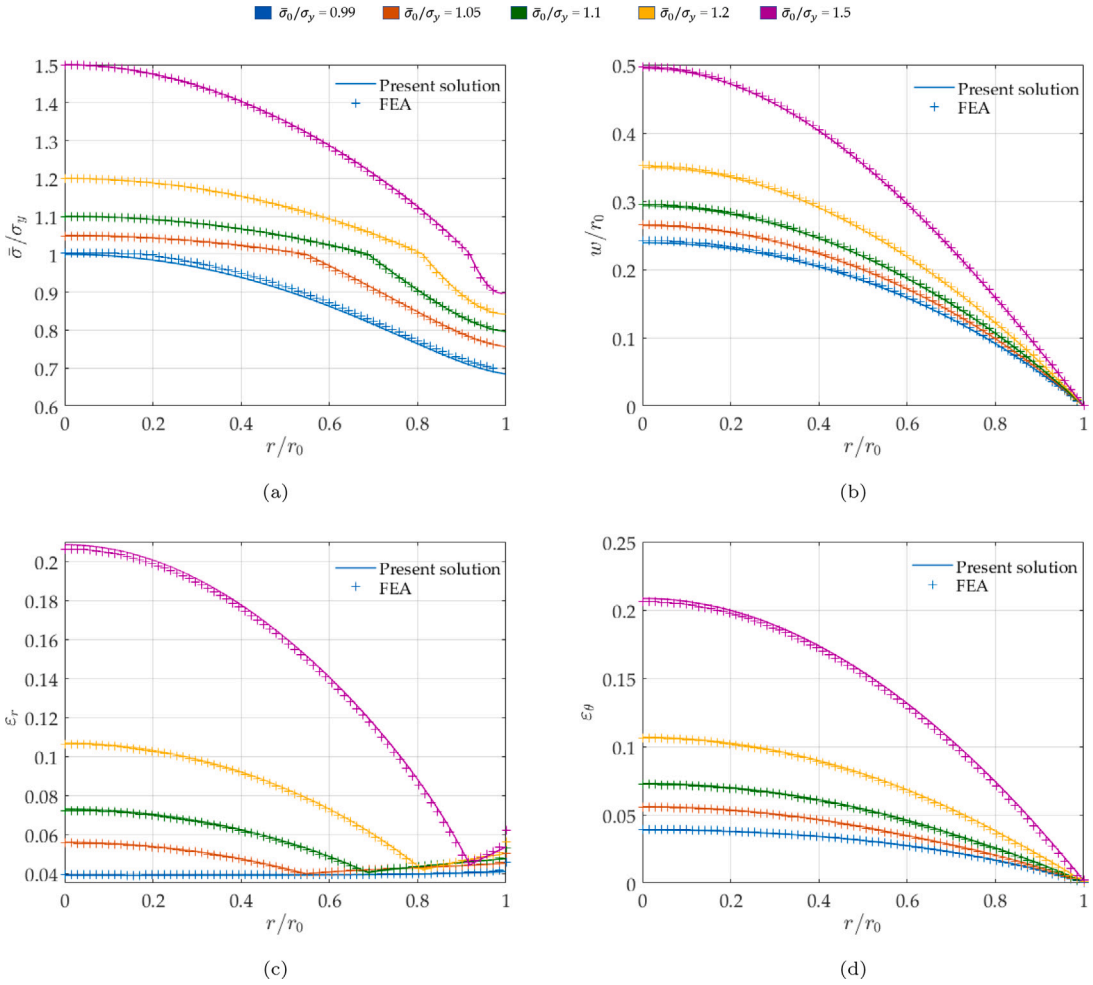

Fig. 3. Radial distribution of (a) normalized equivalent stress $\bar{\sigma}/\sigma_y$, b) vertical displacement w/r_0, (c) radial strain ε_r and (d) circumferential strain ε_θ for $\bar{\sigma}_0/\sigma_y = [0.99, 1.05, 1.1, 1.2, 1.5]$, obtained from FE (+) and current (—) results for the inflation of a circular membrane.

and a non-pronounced change in tangent stiffness at the onset of plasticity. For this reason, in Section 3.2.1, we show that the change in strain distribution during the bulge test can still be experimentally observed and measured in ETFE, which shows nonlinearities close to the yield point. Similarly to the previous plots, the excellent match between the present results and FEA in Figs. 4(a)–4(d) testifies the accuracy of the analytical formulation in the prediction of the inflation response of elastoplastic thin films over the whole spatial domain.

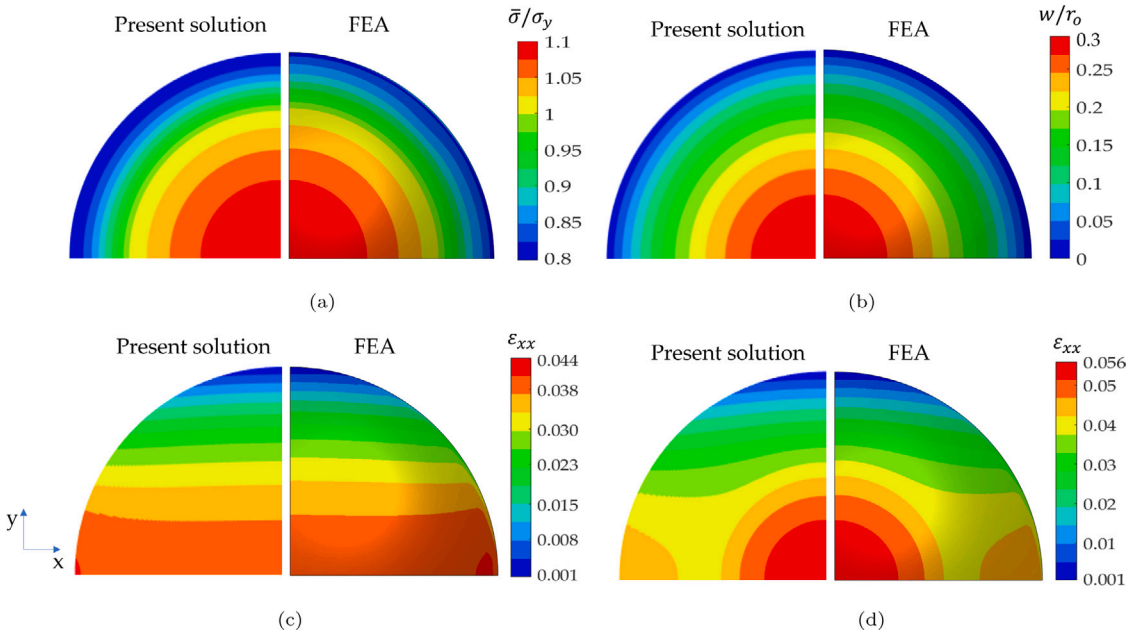

Fig. 4. Comparison between present solution and FE contour plots for (a) normalized equivalent stress $\bar{\sigma}/\sigma_y$, (b) vertical displacement w/r_0 for $\bar{\sigma}_0/\sigma_y = 1.1$, (c) horizontal strain ε_{xx} at $\bar{\sigma}_0/\sigma_y = 0.99$ and (d) $\bar{\sigma}_0/\sigma_y = 1.05$, where $\bar{\sigma}_0$ is the equivalent stress at the apex of the membrane.

3.2. Bulge testing of elastoplastic materials

The following sections report the experimental validation of the presented formulation, thus complementing the numerical validation and showing that it is applicable to different classes of materials and constitutive models, such as linear and nonlinear hardening. In particular, EFTE was chosen because it shows an almost bilinear elastoplastic response, whereas aluminium foil was selected to demonstrate the applicability of the proposed elastoplastic bulging solution to elastic nonlinear-plastic materials.

3.2.1. Diaphragm inflation of a bilinear material

ETFE membranes of 200 μm thickness (Nowoflon ET6235Z-0200-1550-natu8001-0 from Nowofol) were chosen to test the accuracy of the analytical framework during inflation experiments as they closely resembles a bilinear elastoplastic response. The polymeric nature of ETFE makes it a thermo-visco-elasto-plastic material that should not be treated as a von Mises hardening material when the entire thermo-mechanical behaviour is considered. However, the following uniaxial and bulge tests were carefully carried out at the same temperature and strain rate conditions in order to avoid any discrepancy stemming from thermal and deformation rate effects. Therefore, in the context of this section objective, by restricting the attention to ambient temperature and a specific strain rate, ETFE can be modelled as a bilinear von Mises material until ≈12% uniaxial strain (Galliot and Luchsinger, 2011; Coelho, 2012).

First, uniaxial tensile tests were performed to characterize the ETFE response at a specific thermal and deformation rate condition and determine its elastic and plastic material parameters. Uniaxial specimens were cut into the dumbbell shape according to ASTM D412-16 (Type A). An Instron 5985 electromechanical testing machine, fitted with 2 kN 2713-004 self-tightening grips and a 500 N load cell, was used to test the material. The logarithmic strains were measured through digital image correlation (DIC) technique, where two stereo 5 MP cameras (Basler), equipped with Schneider Kreuznach Xenoplan lenses (focal length 35 mm), were held at ≈30° angle and aligned in the loading direction of the specimen. The images were captured from the cameras using Vic-Snap and were post-processed on Vic-3D (Correlated Solutions). The tests were performed in two orthogonal directions of the material to inspect anisotropy. Since a negligible difference (<5%) was observed in the stress–strain response along the extrusion and transverse directions, the material can be considered isotropic (Galliot and Luchsinger, 2011). The typical setup of uniaxial tests is shown in Fig. 5(a).

Table 1
Material properties of 200 μm ETFE membrane, obtained from uniaxial tensile tests.

Elastic modulus E	Yield strength σ_y	Plastic modulus H	Poisson's ratio ν
916.8 MPa	12.4 MPa	117.6 MPa	0.43

The mean true stress–strain curve, $\sigma - \varepsilon$, calculated from three uniaxial tensile tests of ETFE films is shown in Fig. 6 along with the experimental data. The strain rate for these tests was kept in the range 0.005-0.01%/s, which corresponds to the strain rate at the apex of the membrane during the inflation tests while showing negligible strain rate effects. From Fig. 6, it can be observed that ETFE shows a bilinear response only up to ≈12% uniaxial strain, beyond which a nonlinear plastic response begins, which was ignored as its characterization and modelling are outside the scope of this section. Hence, the attention was restricted to the range of strains wherein ETFE shows a bilinear response, and its material properties, extracted from the uniaxial stress–strain curve, are listed in Table 1. The elastic and plastic moduli are found by calculating the slopes of the lines fitting the elastic and plastic phases, respectively, and the yield strength is obtained from the intersection of these two lines, also known as the geometrical method. The Poisson's ratio in the elastic regime, $\nu = 0.43$, is found from the transverse and longitudinal strains measured with DIC during uniaxial tensile tests. The elastic and plastic material properties were employed in the Matlab code to obtain the diaphragm inflation response up to a maximum true stress of ≈ 27 MPa, beyond which the plastic response of EFTE becomes highly nonlinear.

For the diaphragm inflation test, a custom-made pressure chamber was used to clamp the membrane, as shown in Fig. 5(b). The pressure chamber has a circular inner cut of 100 mm diameter. The membrane is clamped at its periphery through fasteners. Additionally, the chamber has an inlet port for air pressure and LED lights inside to illuminate the background of the transparent membrane for DIC measurements.

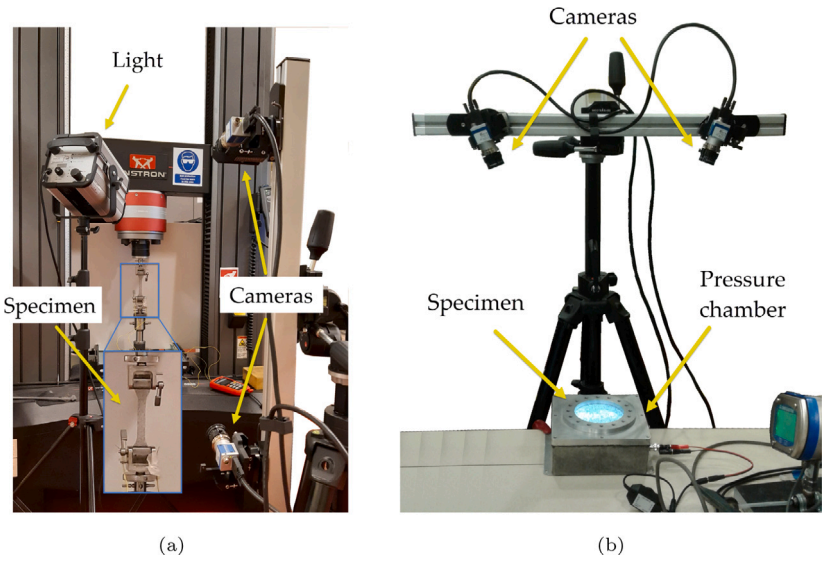

Fig. 5. Experimental setup for (a) uniaxial tensile tests and (b) diaphragm inflation tests.

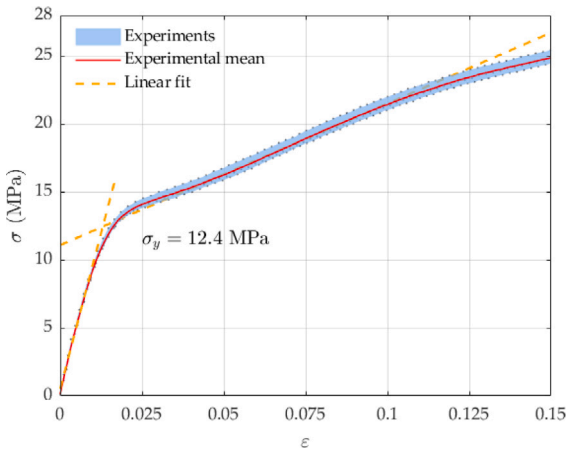

Fig. 6. True stress–strain curve of 200 μm ETFE membranes from uniaxial tensile tests, showing average and raw data along with linear fits of elastic and plastic phases, and the yield strength obtained through the geometrical method.

The high-pressure air is supplied to the testing system and is controlled by an onboard electrically controlled valve (Omega IP610-030) that regulates output air pressure in the range 0-30 psi. The pressure control valve uses 4-20 mA of current generated by an onboard circuitry that includes a DC power supply and a current transmitter AD694. The transmitter converts 0–10 V DC analogue voltage from the computer, provided through the data acquisition system (DAQ) and a LabVIEW Signal Express script, to 4–20 mA of current. An electrical pressure gauge (Omega DPG409-015G) is used to display and send the pressure data of the chamber to the computer through the same DAQ in the form of 0–10 V analogue voltage. It should be noted that the maximum pressure achievable by the pressure gauge and regulator prevented the experiments from reaching large plastic strains (validated through the previous comparison with FEA) or testing thicker sheets.

The stresses in the principal directions of the inflated membrane were calculated by using equilibrium in the normal and vertical directions for an axisymmetric geometry. The equilibrium equations require the pressure values, principal curvatures and the deformed thickness of the membrane as inputs. The vertical equilibrium is given by Eq. (2), where the term $\xi\sqrt{1+\left(\frac{dw}{d\xi}\right)^2}\Big/\frac{dw}{d\xi}$ represents the second principal curvature r_2. Eq. (2) is rewritten in terms of r_2 as

$$\sigma_r = \frac{pr_2}{2h}. \tag{26}$$

The normal equilibrium in terms of principal curvatures r_1 and r_2 is given by (Machado et al., 2012)

$$\frac{\sigma_r}{r_1} + \frac{\sigma_\theta}{r_2} = \frac{p}{h}. \tag{27}$$

The principal curvatures and the strains for the whole membrane were extracted from the DIC measures, while the deformed thickness h is evaluated from Eq. (5) assuming incompressibility.

Three inflation tests on ETFE films were performed, and the results are presented in Fig. 7 along with the predictions from the developed analytical formulation. The high repeatability and low uncertainty of the experimental results are evident by the narrow band of the experimental data in all plots of Fig. 7. The vertical displacement at the apex, normalized by the outer radius of the membrane w/r_0 is plotted against the non-dimensional pressure pr_0/Eh_0 in Fig. 7(a) for both the theoretical and experimental results. The results show a very good agreement as the mathematically-derived curve follows the same trend as the data, with the minor difference caused by an initial displacement offset. The radial strain and the equivalent stress at the apex of the membrane, ε_0 and $\bar{\sigma}_0$, are plotted against the non-dimensional pressure in Figs. 7(b) and 7(c), respectively. Due to the axisymmetry, the radial and circumferential strains at the apex are equal. Therefore, the results are plotted for only one component. The theoretical curves from Fig. 7(c) match closely with the experimental results, whereas they deviate when $\varepsilon_0 \gtrapprox 5\%$ in Fig. 7(b). Such deviation of equibiaxial strain at the apex corresponds to the onset of nonlinear plastic response shown in Fig. 6, further evident in the equivalent stress vs radial strain plot, Fig. 7(d). The sharp change in stiffness at $pr_0/Eh_0 \approx 0.005$, observable in the theoretical curves of Figs. 7(b)–7(d), represents the yield point, while the experimental results follow a smooth transition from elastic to plastic phases, as depicted in the uniaxial stress–strain response of ETFE films, Fig. 6. Overall, the results show the ability of the developed model to accurately predict the bulging of ETFE membranes within the range of strains in which the material can be modelled as bilinear, with a maximum error for the radial strain at the apex of the membrane limited to 7.6%, which occurs at $pr_0/Eh_0 = 0.028$.

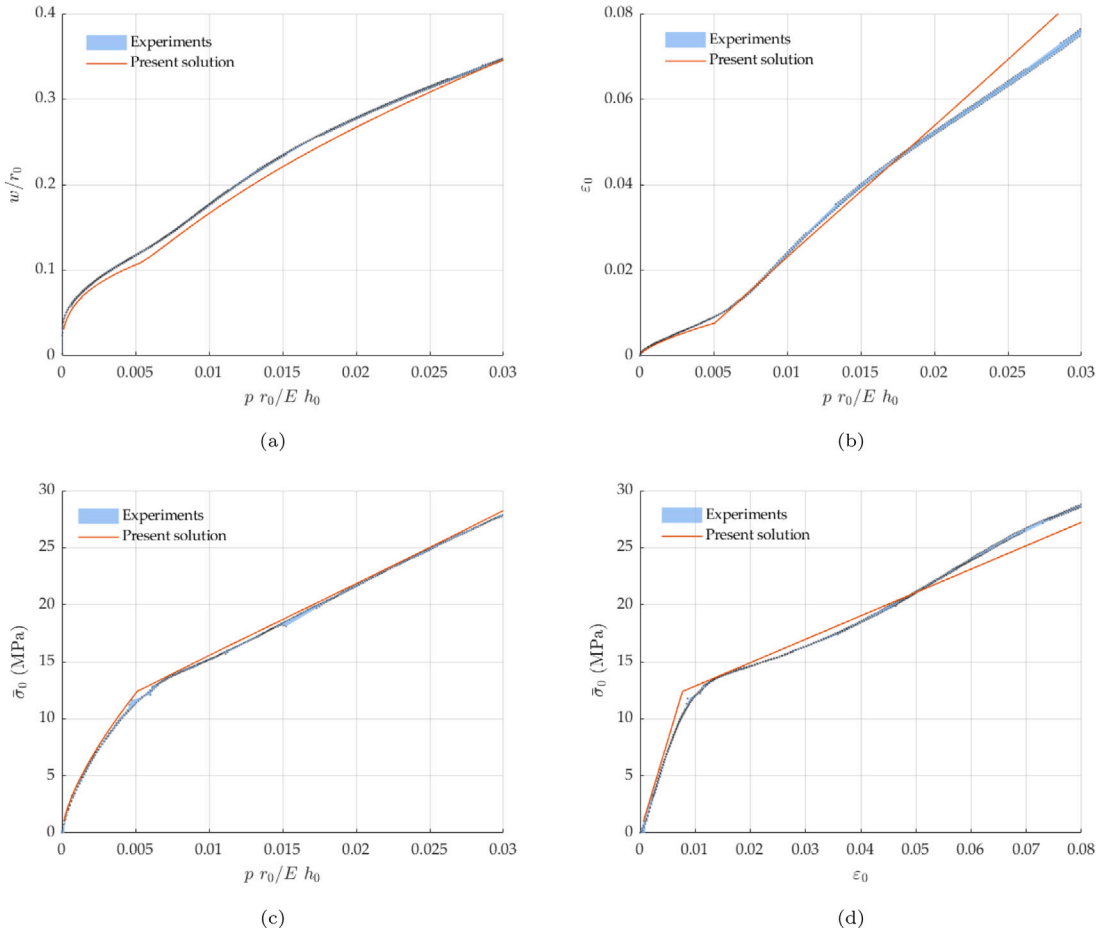

Fig. 7. Comparison between theoretical and experimental results for the diaphragm inflation of ETFE membranes. (a) Normalized vertical displacement w/r_0, (b) strain ε_0 and (c) equivalent stress $\bar{\sigma}_0$ at the apex of the membrane plotted against non-dimensional pressure pr_0/Eh_0. (d) Equivalent stress $\bar{\sigma}_0$ vs radial strain ε_0 at the apex of the membrane.

In addition to the results extracted at the apex of the membrane, the full-field DIC plots of horizontal strain ε_{xx} obtained during ETFE inflation are compared with the theoretical contour plots in Fig. 8, for four instants before and after the onset of plasticity, i.e. $\bar{\sigma}_0/\sigma_y \approx [0.8, 0.99, 1.03, 1.2]$. In the elastic regime, Figs. 8(a) and 8(b), the maximum strain occurs at the edge of the diaphragm, $r = r_0$, while the snapshots were taken in the plastic phase, $\bar{\sigma}_0/\sigma_y \approx [1.03, 1.2]$ in Figs. 8(c) and 8(d), show that the location of maximum strain shifts to the apex of the membrane, $r = 0$, in both theoretical and experimental results. The strain localization at the onset of plasticity from ETFE bulge tests is analogous to the sudden increase in strain at the apex of the membrane observed in the comparison between the present results and FEA, Figs. 4(c) and 4(d). This suggests that plastic strain localization can be experimentally captured during bulge tests through DIC, even for materials showing nonlinearities around the yield point, and it could be further exploited to measure the onset of plasticity in certain membrane materials by means of inflation experiments. The excellent match between experimental data and theoretical strain contours over the entire membrane further proves the accuracy of the developed mathematical formulation, while the small variations in the experimental results of Fig. 8 are due to the intrinsic noise of DIC measurements. However, the noise and uncertainty associated with DIC measurements, which are in the order of ±0.001% for strains (Robert et al., 2007), do not hinder the experimental observation of the onset of plasticity through the highlighted change in strain distribution, and they are negligible since the value is orders of magnitude lower than the yield strain, even for materials that develop plasticity at small strains, such as ETFE or aluminium foil.

3.2.2. Diaphragm inflation of a linear elastic-nonlinear plastic material

The validation of the analytical formulation is extended to include materials that can differ from an ideal bilinear elastoplastic behaviour. Although the analytical formulation is presented for a constant plastic modulus H, it has the ability to capture nonlinear hardening and incorporate variable plastic modulus, defined as a function of equivalent stress $\bar{\sigma}$. Additional details on the implementation of the hardening law H are given in Appendix A. Aluminium foils 8079 (from Hollinbrow Precision Products ltd) of 25 μm thickness were chosen for the experimental validation as they show a linear elastic-nonlinear plastic response and they can be tested until failure with the custom bulge test setup. The experimental procedure and equipment were the same as described in the previous section for ETFE. Three uniaxial tensile tests were performed to characterize the material response and determine its parameters. They were carried out along the foil rolling direction and its perpendicular direction, to assess any orthotropic effect on the mechanical response. The difference in uniaxial response between the two directions resulted lower than 3% and 8% in the elastic and plastic phases, respectively, and therefore was neglected, thus considering the material as isotropic. The mean true stress–strain curve from uniaxial tensile tests of aluminium foil is shown in Fig. 9. The uniaxial tests for aluminium foils were carried out at strain rates 0.01 − 0.025%/s, until failure. The tested foil shows an almost perfectly plastic response beyond ε =1%, until a failure strain of ≈ 3%. The small strain at failure is attributed to the hard condition of the aluminium foil due to the rolling process, coupled with the thickness effect, which was shown to decrease ductility and reduce failure strain as the foil thickness is reduced (Espinosa et al., 2004; Simons et al., 2006). Compared with

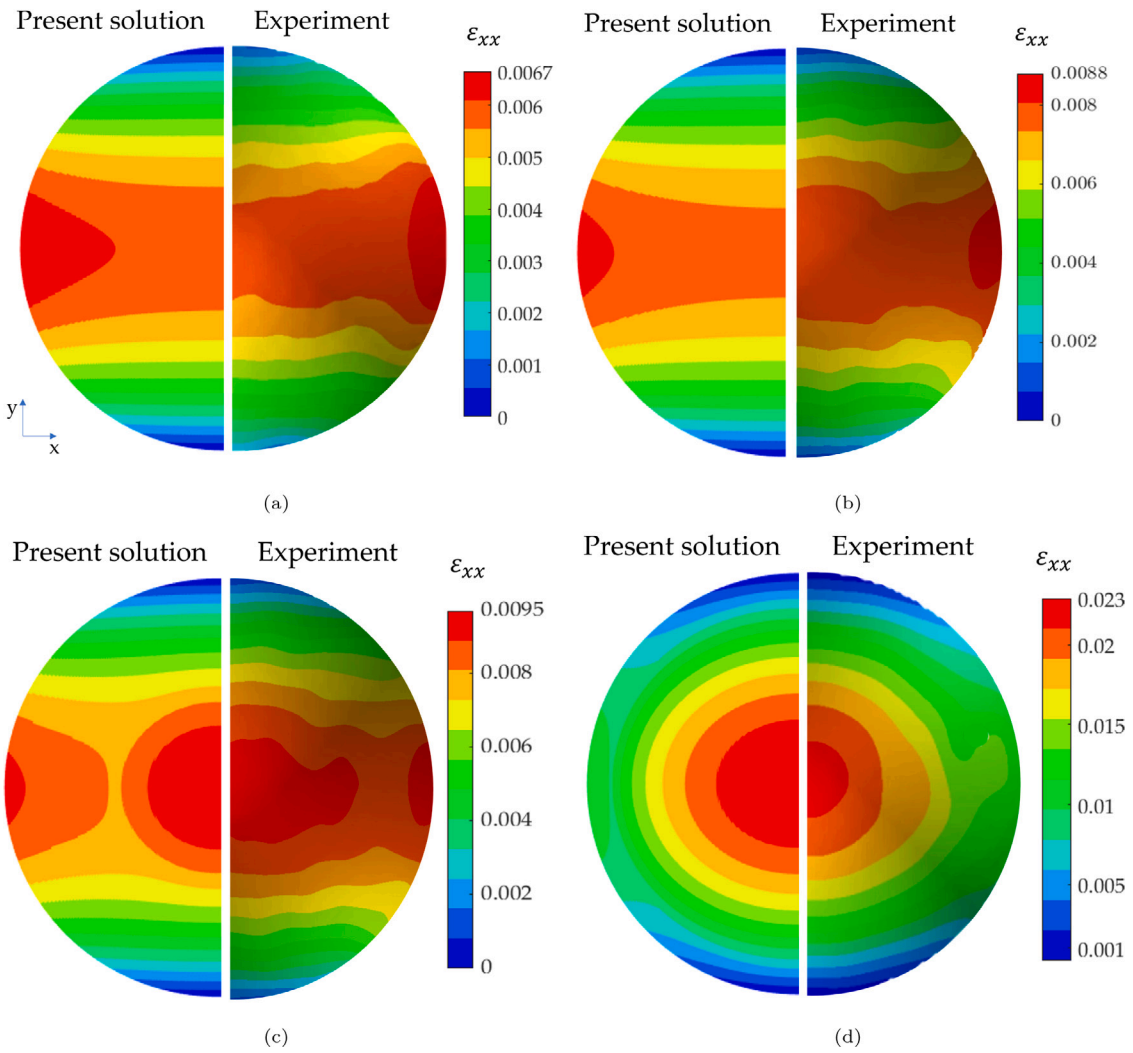

Fig. 8. Theoretical and experimental contour plots of horizontal strain ϵ_{xx} at (a) $\bar{\sigma}_0/\sigma_y = 0.8$, (b) $\bar{\sigma}_0/\sigma_y = 0.99$, (c) $\bar{\sigma}_0/\sigma_y = 1.03$ and (d) $\bar{\sigma}_0/\sigma_y = 1.2$ during ETFE inflation, where $\bar{\sigma}_0$ is the equivalent stress at the apex of the membrane and σ_y is the yield stress.

Table 2
Material properties of 25 μm aluminium foils, obtained from uniaxial tensile tests.

Elastic modulus	Yield strength	Poisson's ratio	Ramberg–Osgood parameters	
E	σ_y	ν	α	n
55 GPa	110 MPa	0.37	3×10^{-4}	19.3

ETFE experimental data, the higher standard deviation observable on aluminium foils, especially in the plastic phase, is caused by the high stiffness of the material, which increases the variability of DIC strain measurements at very small strains, and by the higher, yet negligible, material orthotropy in the plastic phase.

The material properties extracted from the experimental uniaxial stress–strain curve are listed in Table 2, where the elastic modulus E is found by linear regression of the stress–strain data in the elastic phase. Due to the nonlinearity of the material, the yield strength σ_y was obtained through strain recovery tests (Bosi and Pellegrino, 2017). In that procedure, a series of uniaxial loading and unloading tests were performed by increasing by 5 MPa the maximum stress value reached during loading, until non-negligible residual deformations after unloading (>0.02%) were measured; that value of stress was considered the yield stress of the material. The equivalent stress-dependent plastic

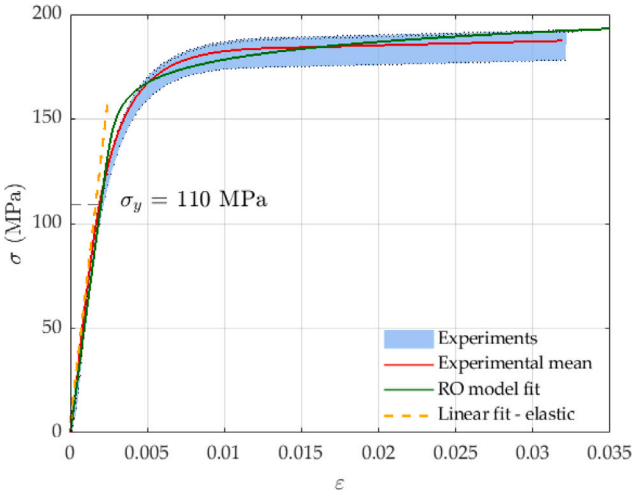

Fig. 9. True stress–strain curve of 25 μm aluminium foils from uniaxial tensile tests until failure, showing average and raw data along with the linear fit of the elastic regime and the yield strength obtained through the strain recovery method. The green curve represents the Ramberg–Osgood (RO) model fit.

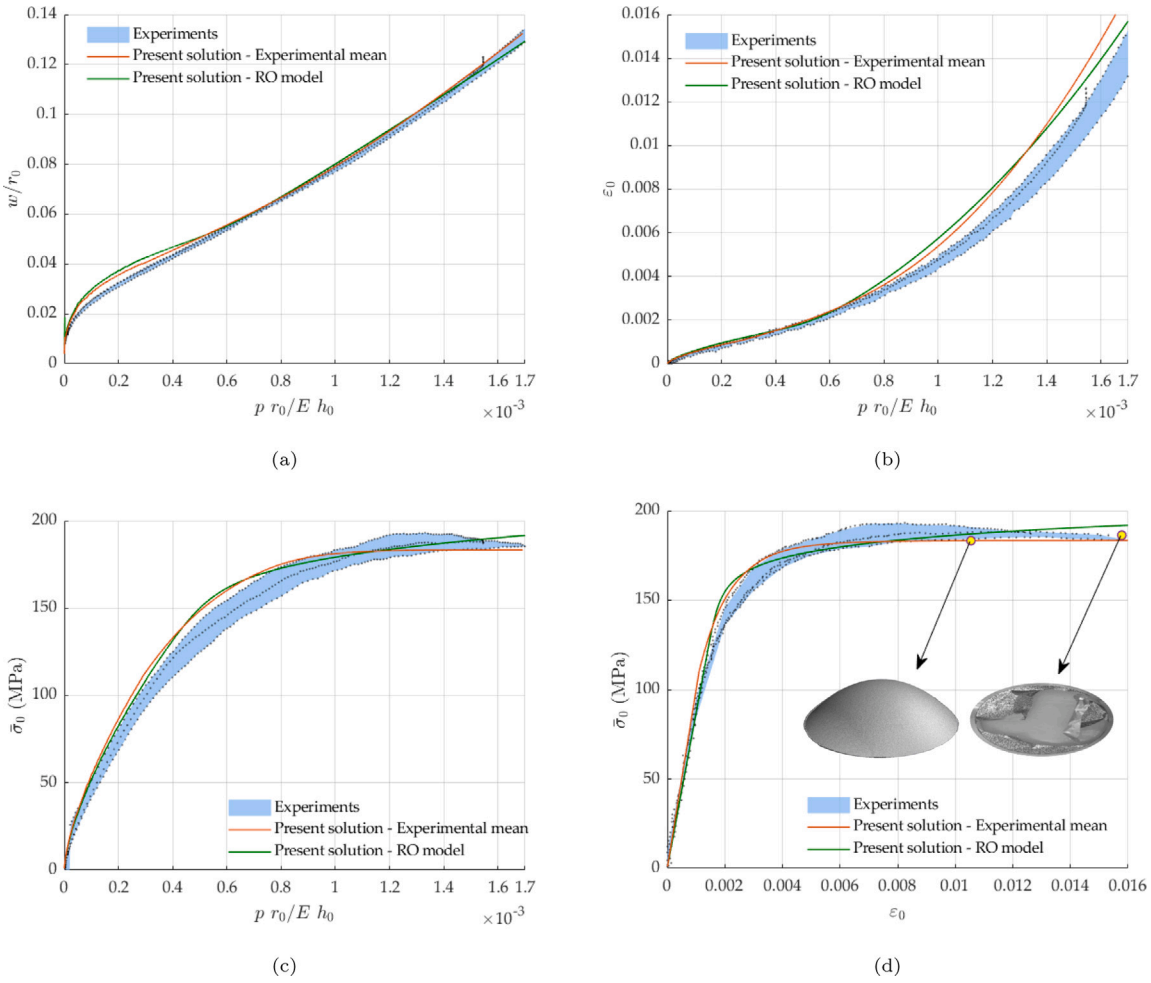

Fig. 10. Comparison between theoretical and experimental results for the diaphragm inflation of aluminium foils. The theoretical results are obtained using the uniaxial mean experimental data (red curve) and Ramberg–Osgood model (green curve) as input for the developed code. (a) Normalized vertical displacement w/r_0 and (b) strain ε_0, (c) equivalent stress $\bar{\sigma}_0$ at the apex of the foil plotted against non-dimensional pressure pr_0/Eh_0. (d) Equivalent stress $\bar{\sigma}_0$ vs radial strain ε_0 at the apex of the foil; insets show the three-dimensional deformed surface of the pressurized film before and at failure.

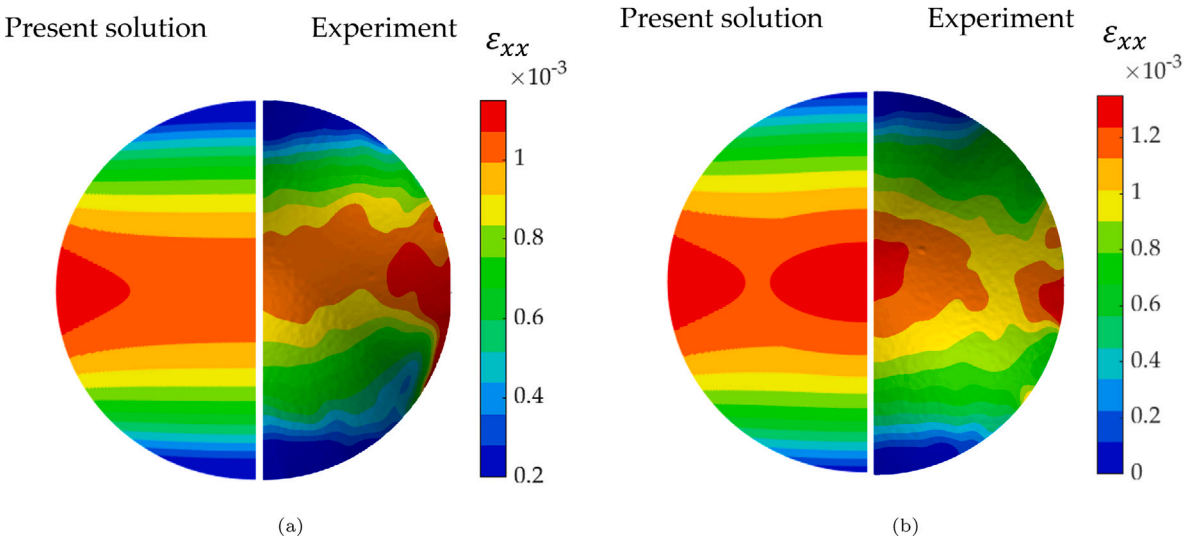

Fig. 11. Theoretical and experimental contour plots of horizontal strain ε_{xx} at (a) $\bar{\sigma}_0/\sigma_y = 0.95$ and (b) $\bar{\sigma}_0/\sigma_y = 1.1$ during aluminium foil inflation, where $\bar{\sigma}_0$ is the equivalent stress at the apex of the membrane and σ_y is the yield stress.

modulus H was determined by calculating the slopes of the tangents of the mean stress–strain curve for each strain level in the plastic region of the two materials, as shown in Appendix A. Additionally, the mean experimental data were employed to model the aluminium foil response through the Ramberg–Osgood (RO) model

$$\varepsilon = \frac{\sigma}{E} + \alpha \frac{\sigma}{E} \left(\frac{\sigma}{\sigma_y} \right)^{n-1}, \tag{28}$$

where α and n are material parameters defining the hardening behaviour. On the right hand side of the former equation, the first and second terms represent the elastic and plastic strains, respectively. The best fit parameters, $\alpha = 3 \times 10^{-4}$ and $n = 19.3$, were found by using the `findfit` function with its `conjugategradient` method, from Wolfram Mathematica (v.11.3). The material properties were used to predict the response of aluminium foil during bulge test, up to failure. Two material models were given as input in the Matlab code to compare their predictions: (i) the mean experimental curve (red curve in Fig. 9) through the measured relationship between stresses and elastic and plastic strains, and (ii) the Ramberg–Osgood model (green curve in Fig. 9).

The results from the experiments and presented theoretical solution for the bulging of aluminium foils are presented in Fig. 10. Three inflation tests were performed until failure, where the speed of the tests was adjusted so that maximum strain rates at the apex of the bulged foils match with those from uniaxial tests for a major portion of the deformation response of the material, as detailed in Appendix B. The experimental setup for aluminium bulge tests is identical to that described in the previous section for ETFE, where the inflating pressure is recorded by the pressure gauge, the kinematic quantities (displacements, strains and curvatures) are measured through DIC, and the stresses at the apex of the foil are calculated by means of Eqs. (26) and (27).

The normalized vertical displacement curves w/r_0 from the analytical solutions are very close to the experiments, except for a slight difference at small pressure, Fig. 10(a). In Fig. 10(b), the theoretical and experimental results for the radial strain at the apex, ϵ_0, are in very good agreement up to $pr_0/Eh_0 \approx 0.0007$, beyond which the increasing difference is attributed to the increase of strain rate in inflation tests after the occurrence of plasticity, which is harder to keep constant under pressure control and makes the material stiffer at higher deformation levels, with a maximum difference of $\approx 13\%$. Further details on the quantification of the increase of strain rate for the inflation tests of aluminium foils are given in Appendix B. The plots of equivalent stress at the apex, $\bar{\sigma}_0$, against non-dimensional load pr_0/Eh_0, Fig. 10(c), and strain at the apex, ϵ_0, Fig. 10(d), confirm the very good agreement between predictions and measurements. For all plots of Fig. 10, it can be noted that the theoretical predictions with the two input models yield similar results, even though the fitting of the uniaxial data can be improved by using another constitutive model, as shown in Appendix C through the Swift-Voce hardening. This suggests that if the uniaxial experimental relationship between stress and strain is known (red curve in Fig. 9), it can be used as a direct input in the developed code to accurately predict the inflation of thin films, without the need for establishing a material model through model fitting, such as the Ramberg–Osgood employed in the green curve of Fig. 9 or the Swift-Voce model shown in Fig. C.14.

Similarly to ETFE experiments, the full-field DIC contours of the horizontal strain ε_{xx} measured during aluminium foil inflation are compared with the theoretical contour plots in Fig. 11 for two instants before and after yielding. As already noted in Sections 3.1 and 3.2.1, when the membrane is in the elastic phase, the strains are maximum at the periphery of the circular region for both the theoretical prediction (left) and experimental measures (right), as shown in Fig. 11(a) for $\bar{\sigma}_0/\sigma_y = 0.95$. In contrast, the strain localizes at the apex when plasticity occurs, as shown in Fig. 11(b) for $\bar{\sigma}_0/\sigma_y = 1.1$. The comparison between predictions and measurements are good despite the increased noise in DIC data, caused by the high stiffness of aluminium foils, which leads to strains that are almost one order of magnitude lower than those of ETFE. The ability to capture plastic strain localization with good accuracy at small strains is of significant importance to the developed formulation and can serve as a mean to study the occurrence of plasticity in various thin film materials.

Overall, the closeness of the mathematically-derived results to the experiments for aluminium foils in Figs. 10 and 11 further validates the finite strain formulation for the circular diaphragm inflation of isotropic nonlinear plastic materials. Improvements to the formulation and its numerical implementation can be developed by extending the presented solution to elastoviscoplastic and viscoelastoplastic materials, or by accounting for material anisotropy (Liu et al., 2015; Reis et al., 2016; Chen et al., 2016, 2018). In the latter scenario, the inflation of circular anisotropic material leads to non-axisymmetric bulged shapes, thus transforming the analysis from 1D to 2D and requiring a different approach (Suleman and Bosi, 2022).

4. Conclusion

A finite strain analytical formulation has been developed for the inflation of plane circular membranes composed of isotropic elastoplastic materials, thus addressing the lack of comprehensive elastoplastic modelling for thin films bulging. The results from the model, obtained through a developed Matlab script made open source, have been compared with finite element analyses, depicting an excellent agreement for a wide range of finite strain and material parameters, namely elastic and $E/H = [2, 5, 10, 20, 50, 100]$. The Poisson's ratio has been found to have a negligible effect on the inflation response compared to the ratio E/H. The mathematical formulation has been proven to predict the deformation of inflatable planar membranes at small and large plastic strains, accurately capturing the plastic strain localization developing at the apex of the films and its subsequent radial increase. This ability to precisely capture the sudden change in full-field strain distribution that occurs at the onset of plasticity could be employed to develop a new experimental procedure to determine the occurrence of plastic deformation and characterize the yield strength of thin-film materials through imaging techniques, such as digital image correlation. Additional analyses and validations are necessary to show the applicability of such procedure to various materials, which will be part of future research efforts. The new formulation has also been experimentally validated through bulge tests carried out on two different membrane materials over a range of thicknesses. In particular, 200 μm ETFE membranes that can be modelled with a bilinear elastoplastic behaviour up to ≈12% strain were tested to assess the mathematical predictions when the plastic modulus is constant and demonstrate the capability of measuring the change in strain distribution at the onset of permanent deformation in the presence of nonlinearities at the yield point. Additionally, the inflation response of 25 μm aluminium foils was characterized to prove the accuracy of the finite strain formulation and its numerical implementation for an elastic-nonlinear plastic material modelled through the Ramberg–Osgood constitutive relation. Overall, a very good agreement has been found between theoretical predictions and experimental measures, with maximum error for the principal stress and strain at the apex found to be under 8% for ETFE membranes and below 13% for aluminium foils. The proposed finite strain formulation, together with its numerical and experimental validations, promises to enhance the elastoplastic modelling and characterization of natural and engineering membranes, especially in (i) capturing the features when elastic and plastic phases coexist in inflated sheets, (ii) modelling the response of materials implemented in inflatable mechanisms and (iii) determining material constants through bulge experiments, one of the most successful procedures to assess the biaxial response of thin films.

Declaration of competing interest

The authors declare that they have no known competing financial interests or personal relationships that could have appeared to influence the work reported in this paper.

Data availability

The developed scripts can be found at https://github.com/fbosi/ElastoplasticDiaphragmBulging. Additional data will be made available on request.

Acknowledgements

The authors thank Alessandro Comitti for performing uniaxial tensile tests on ETFE. F.B. and K.S. acknowledge support from the EU H2020-MSCA-ITN-2020-LIGHTEN-956547.

Appendix A. Hardening law for nonlinear plastic materials

The mathematical formulation presented in Section 2.1 assumes constant hardening modulus H. However, depending on the material behaviour, H can be variable and defined as a function of equivalent stress $\bar{\sigma}$ or equivalent plastic strain ε_p as $H(\bar{\sigma})$ or $H(\varepsilon_p)$, respectively. It can be found from the experimental stress–strain curve of the material by calculating the gradient of the equivalent stress vs. equivalent plastic strain curve, or by differentiating the analytical expression of the Ramberg–Osgood or Swift-Voce material models. As an example, the $\bar{\sigma} - \varepsilon_p$ curve extracted from Fig. 9 is presented in Fig. A.12. The plastic modulus H is given by

$$H = \frac{d\bar{\sigma}}{d\varepsilon_p} \tag{29}$$

where ε_p is calculated by subtracting elastic strain from the total uniaxial strain, $\varepsilon_p = \varepsilon - \varepsilon_e$. In the numerical solution procedure, the value of H is updated for each time step over the whole membrane region, based on the magnitude of $\bar{\sigma}$. It should be noted that during the analytical derivation, Eq. (21) is differentiated with respect to r. However, within the region of the membrane undergoing plasticity, the equivalent stress $\bar{\sigma}$ has a limited variation along the radial coordinate r, as shown in Fig. 3(a). Hence, in order to simplify the numerical procedure, the dependence of $H(\bar{\sigma})$ on r is not considered, and H is assumed constant over the plastic spatial domain. If the time step is sufficiently small, this approach has been validated with finite element analyses on nonlinear hardening materials, showing negligible differences.

Appendix B. Strain rate evolution at the apex of circular bulge tests for aluminium foil

Section 3.2.2 points out that the strain rate at the apex of the membrane increases significantly after the occurrence of plasticity for the inflation of aluminium foils, despite the effort of keeping it as close as possible to the strain rate used for uniaxial tests. Fig. B.13 quantifies the average magnitude of such increase by showing the evolution of the equivalent strain rate $\dot{\varepsilon}$ as a function of the equivalent stress $\bar{\sigma}$ for both uniaxial and inflation tests of aluminium foils. It can be seen that in the elastic phase, the equivalent strain rate during bulge tests matches that of the uniaxial experiments. Subsequently, although the strain rate during inflation test starts to increase at a stress level of $\approx$ 125 MPa, the difference becomes significant after 170 MPa, which corresponds to the stress saturation before failure. The rapid increase of equivalent strain rate can cause localized viscoplastic effects at the apex of the inflated specimen, which can contribute to the deviation between experimental measures and theoretical predictions occurring at high strains and observed in Figs. 10(b) and C.14(b).

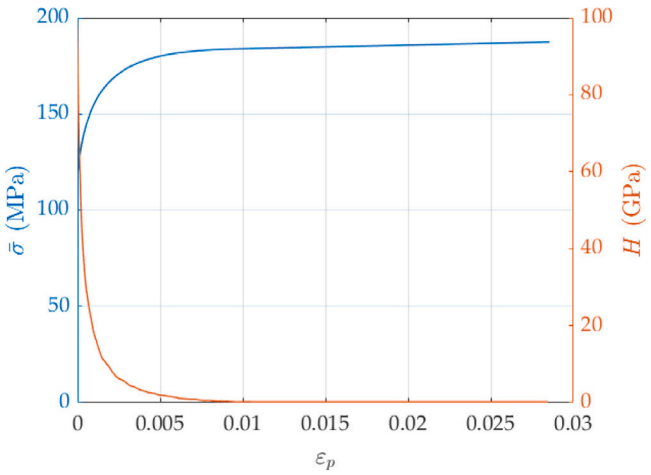

Fig. A.12. Equivalent stress $\bar{\sigma}$ plotted against the equivalent plastic strain ε_p for the plastic phase of aluminium foils, extracted from the uniaxial tensile tests until failure (Fig. 9). The evolution of the plastic modulus H is shown on the right axis..

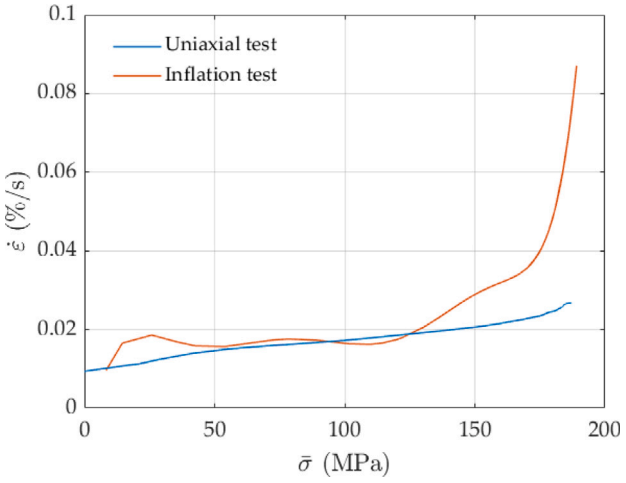

Fig. B.13. Mean value of equivalent strain rate $\dot{\varepsilon}$ vs equivalent stress $\bar{\sigma}$ from uniaxial and bulge tests for aluminium foils..

Table C.3
Best fit material parameters for Swift-Voce model obtained from uniaxial tensile tests of 25 μm aluminium foils.

ρ	a	k	b	m	c
0.47	10^{-6}	216 MPa	77.4 MPa	0.04	703

Appendix C. Swift-voce hardening model for aluminium foil

The mixed form of Swift and Voce hardening is expressed as a relationship between the equivalent stress $\bar{\sigma}$ and the equivalent plastic strain ε_p given by (Chen et al., 2018)

$$\bar{\sigma} = \rho\left[k(a+\varepsilon_p)^m\right] + (1-\rho)\left[\sigma_y + b(1-e^{-c\ \varepsilon_p})\right] \tag{30}$$

where the first quantity on the right-hand side represents Swift hardening, the second is the Voce model, and ρ is the weight factor of the rule of mixture. The best fit model parameters a, b, c, k and m, reported in Table C.3, were obtained in Wolfram Mathematica (v.11.3) through the same procedure employed for the Ramberg–Osgood (RO) fitting. The calibrated parameters enable the excellent match between the uniaxial experimental mean and the SV model, which significantly improves the fitting provided by the RO model, as shown in Fig. C.14(a). The SV model was used in the developed code to predict the response of

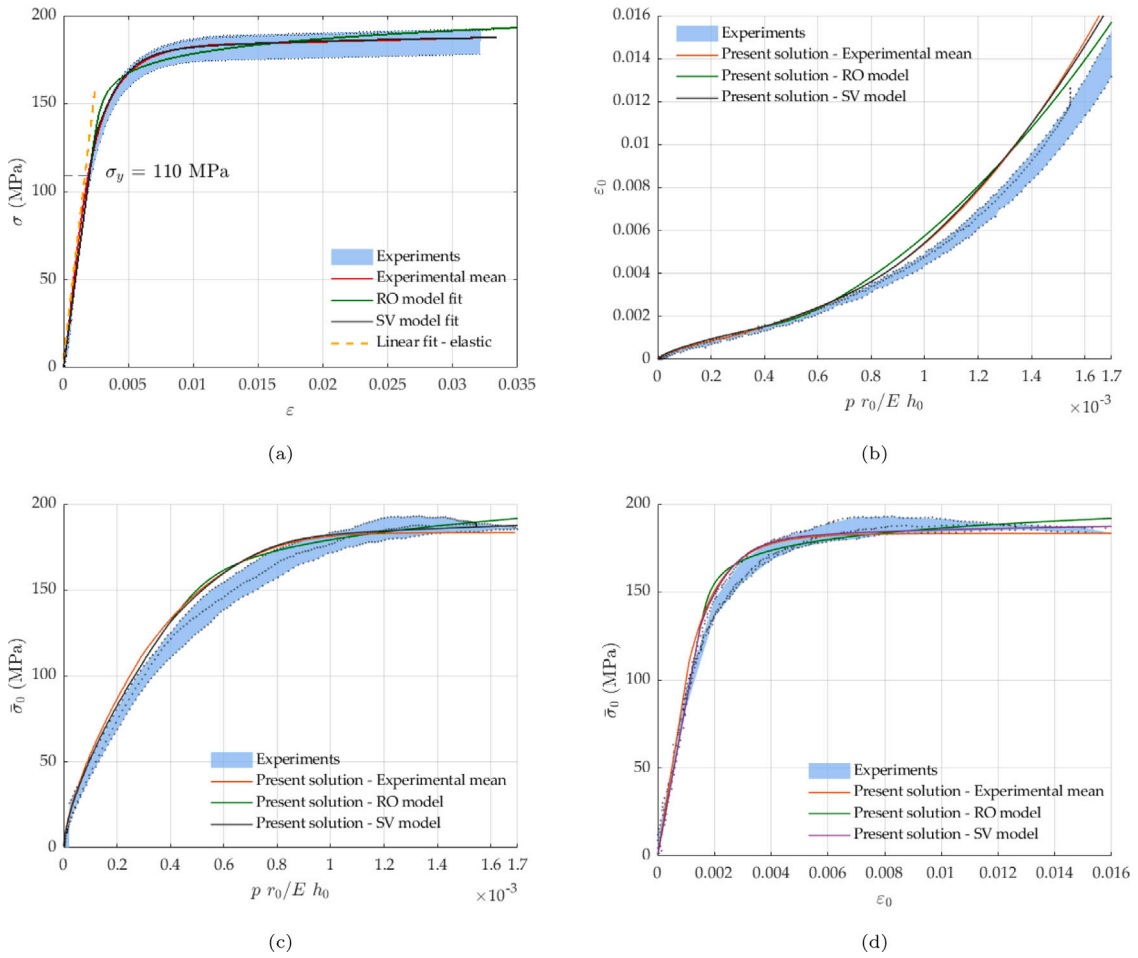

Fig. C.14. (a) True stress–strain curve of 25 μm aluminium foils from uniaxial tensile tests until failure, showing average (red curve) and raw data along with the linear fit of the elastic region (dashed yellow line), Ramberg–Osgood (RO, green curve) and Swift-Voce (SV, black curve) model fits. The theoretical results for the inflation of aluminium foils are obtained using the uniaxial mean experimental data, RO and SV models as input for the developed code, and they are compared with experimental results for (b) strain ϵ_0 and (c) equivalent stress $\bar{\sigma}_0$ at the apex of the foil vs non-dimensional pressure pr_0/Eh_0, and (d) equivalent stress $\bar{\sigma}_0$ vs radial strain ϵ_0 at the apex of the foil.

aluminium foil during inflation, which is reported in Figs. C.14(b)–C.14(d) and is compared with the experimental response and RO model previously presented in Fig. 10. It can be noted that the improved fitting given by the SV model through the higher number of parameters closely matches the one obtained when the mean experimental response is used as input in the code. As observed before for Fig. 10, the predicted response is overall in very good agreement with the experimental measurements except beyond $pr_0/Eh_0 \approx 0.0007$ in Fig. C.14(b), which is attributed to the sudden increase of strain rate observable towards the stress saturation and described in Appendix B.

References

Adkins, J.E., Rivlin, R.S., 1952. Large elastic deformations of isotropic materials IX. The deformation of thin shells. Philos. Trans. R. Soc. Lond. Ser. A Math. Phys. Eng. Sci. 244, 505–531.

Benet, E., Zhu, H., Vernerey, F.J., 2019. Interplay of elastic instabilities and viscoelasticity in the finite deformation of thin membranes. Phys. Rev. E 99, 042502 (1–12).

Bosi, F., Pellegrino, S., 2017. Molecular based temperature and strain rate dependent yield criterion for anisotropic elastomeric thin films. Polymer 125, 144–153.

Bosi, F., Pellegrino, S., 2018. Nonlinear thermomechanical response and constitutive modeling of viscoelastic polyethylene membranes. Mech. Mater. 117, 9–21.

Campbell, J.D., 1956. On the theory of initially tensioned circular membranes subjected to uniform pressure. Quart. J. Mech. Appl. Math. 9, 84–93.

Chaudhuri, A., DasGupta, A., 2014. On the static and dynamic analysis of inflated hyperelastic circular membranes. J. Mech. Phys. Solids 64, 302–315.

Chen, K., 2020. A general and unified theory of the kinematic relationships in bulge tests. J. Mech. Phys. Solids 143, 104086.

Chen, K., Scales, M., Kyriakides, S., 2018. Material hardening of a high ductility aluminum alloy from a bulge test. Int. J. Mech. Sci. 138–139, 476–488.

Chen, K., Scales, M., Kyriakides, S., Corona, E., 2016. Effects of anisotropy on material hardening and burst in the bulge test. Int. J. Solids Struct. 82, 70–84.

Coelho, M.A., 2012. Analysis of pneumatic structures considering nonlinear material models and pressure-volume couppling (Ph.D. thesis). Pontificia Universidade Catolica do Rio de Janeiro.

Coelho, M., Roehl, D., Kai-UweBletzinger, 2014. Numerical and analytical solutions with finite strains for circular inflated membranes considering pressure–volume coupling. Int. J. Mech. Sci. 82, 122–130.

Diehl, A., Engel, U., Geiger, M., 2008. Mechanical properties and bending behaviour of metal foils. Proc. Inst. Mech. Eng. B 222 (1), 83–91.

Emery, D., Fu, Y., 2021. Localised bifurcation in soft cylindrical tubes under axial stretching and surface tension. Int. J. Solids Struct. 219, 23–33.

Espinosa, H., Prorok, B., Peng, B., 2004. Plasticity size effects in free-standing submicron polycrystalline FCC films subjected to pure tension. J. Mech. Phys. Solids 52 (3), 667–689.

Fichter, W.B., 1997. Some solutions for the large deflection of uniformly loaded circular membranes. Technical Report, NASA Langley Research Center; Hampton, VA United States.

Foster, H.O., 1967a. Inflation of a plane circular membrane. J. Eng. Ind. 89 (3), 403–407.

Foster, H.O., 1967b. Very large deformation of axially symmetrical membranes made of neo-hookean materials. Internat. J. Engrg. Sci. 5, 95–117.

Fox, J.W., Goulbourne, N.C., 2008. On the dynamic electromechanical loading of dielectric elastomer membranes. J. Mech. Phys. Solids 56, 2669–2686.

Galliot, C., Luchsinger, R., 2011. Uniaxial and biaxial mechanical properties of ETFE foils. Polym. Test. 30 (4), 356–365.

Green, A.E., Zerna, W., 1968. Theoretical Elasticity, second ed. Oxford University Press.

Hencky, H., 1915. On the stress state in circular plates with vanishing bending stiffness. Z. Fiir Math. Phys. 63, 311–317.

Hill, R., 1950. A theory of the plastic bulging of a metal diaphragm by lateral pressure. Lond. Edinb. Dublin Philos. Mag. J. Sci. 41, 1133–1142.
Inoue, K., Owaki, T., Nakamura, T., Kitamura, F., Miyamoto, N., 1984. Clinical application of transvenous mitral commissurotomy by a new balloon catheter. J. Thorac. Cardiovasc. Surg. 87, 394–402.
Jin, L., Forte, A.E., Deng, B., Rafsanjani, A., Bertoldi, K., 2020. Kirigami-inspired inflatables with programmable shapes. Adv. Mater. 32, 2001863 (1–7).
Koch, K.M., 2004. Membrane Structures: Innovative Building with Film and Fabric. Prestel Pub.
Li, M., Ranzani, T., Sareh, S., Seneviratne, L.D., Dasgupta, P., Wurdemann, H.A., Althoefer, K., 2014. Multi-fingered haptic palpation utilizing granular jamming stiffness feedback actuators. Smart Mater. Struct. 23, 095007.
Lian, Y.S., Sun, J.Y., Yang, Z.X., He, X.T., Zheng, Z.L., 2016. Closed-form solution of well-known Hencky problem without small-rotation-angle assumption. J. Appl. Math. Mech. 96, 1434–1441.
Lim, T.-C., 2016. Large deflection of circular auxetic membranes under uniform load. J. Eng. Mater. Technol. 138 (4), 041011 (1–7).
Liu, K., Lang, L., Cai, G., Yang, X., Guo, C., Liu, B., 2015. A novel approach to determine plastic hardening curves of AA7075 sheet utilizing hydraulic bulging test at elevated temperature. Int. J. Mech. Sci. 100, 328–338.
Love, A.E.H., 1927. A Treatise on the Mathematical Theory of Elasticity, fourth ed. Cambridge University Press.
Machado, G., Favier, D., Chagnon, A.G., 2012. Membrane curvatures and stress-strain full fields of axisymmetric bulge tests from 3D-DIC measurements. Theory and validation on virtual and experimental results. Exp. Mech. 52, 865–880.
McCrum, N.G., Buckley, C.P., Bucknall, C.B., 1997. Principles of Polymer Engineering, second ed. Oxford Science Publications.
Melzer, M., Kaltenbrunner, M., Makarov, D., Karnaushenko, D., Karnaushenko, D., Sekitani, T., Someya, T., Schmidt, O.G., 2015. Imperceptible magnetoelectronics. Nature Commun. 6, 1–8.
Mooney, M., 1940. A theory of large elastic deformation. J. Appl. Phys. 11, 582–592.
Needleman, A., 1976. Necking of pressurized spherical membranes. J. Mech. Phys. Solids 24, 339–359.
Rausch, M.K., Kuhl, E., 2014. On the mechanics of growing thin biological membranes. J. Mech. Phys. Solids 63, 128–140.
Rees, D., 1995. Plastic flow in the elliptical bulge test. Int. J. Mech. Sci. 37 (4), 373–389.
Reis, L., Oliveira, M., Santos, A., Fernandes, J., 2016. On the determination of the work hardening curve using the bulge test. Int. J. Mech. Sci. 105, 158–181.
Rivlin, R.S., 1948. Large elastic deformations of isotropic materials IV. Further developments of the general theory. Philos. Trans. R. Soc. Lond. Ser. A Math. Phys. Eng. Sci. 241, 379–397.
Robert, L., Nazaret, F., Cutard, T., Orteu, J.-J., 2007. Use of 3-D digital image correlation to characterize the mechanical behavior of a fiber reinforced refractory castable. Exp. Mech. 47, 761–773.
Rossi, M., Lattanzi, A., Barlat, F., Kim, J.-H., 2022. Inverse identification of large strain plasticity using the hydraulic bulge-test and full-field measurements. Int. J. Solids Struct. 111532.
Shepherd, R.F., Ilievski, F., Choi, W., Morin, S.A., Stokes, A.A., Mazzeo, A.D., Chen, X., Wang, M., Whitesides, G.M., 2011. Multigait soft robot. Proc. Natl. Acad. Sci. 108, 20400–20403.
Siéfert, E., Bico, J., Reyssat, E., Roman, B., 2020. Geometry and mechanics of inextensible curvilinear balloons. J. Mech. Phys. Solids 143, 104068.
Simons, G., Weippert, C., Dual, J., Villain, J., 2006. Size effects in tensile testing of thin cold rolled and annealed Cu foils. Mater. Sci. Eng. A 416, 290–299.
Strong, A.B., 2006. Plastics: Materials and Processing, third ed. Pearson, Upper Saddle River, USA.
Suleman, K., Bosi, F., 2022. Direct stress computations in arbitrarily shaped thin shells and elliptic bulge tests. Proc. R. Soc. Lond. Ser. A Math. Phys. Eng. Sci. 478 (2268), 20220619.
Tinoco, H.A., Hutar, P., Kruml, T., Holzer, J., 2021. Modeling of elastoplastic behavior of freestanding square thin films under bulge testing. Acta Mech. 232, 2715–2731.
Wang, S., Guo, Z., Zhou, L., Li, L., Fu, Y., 2019. An experimental study of localized bulging in inflated cylindrical tubes guided by newly emerged analytical results. J. Mech. Phys. Solids 124, 536–554.
Wang, N.M., Shammamy, M.R., 1969. On the plastic bulging of a circular diaphragm by hydrostatic pressure. J. Mech. Phys. Solids 17, 43–61.
Xiang, Y., Chen, X., Vlassak, J., 2005. Plane-strain bulge test for thin films. J. Mater. Res. 20 (9), 2360–2370.
Yadav, M., Chiu, F.C., 2019. Cellulose nanocrystals reinforced κ-carrageenan based UV resistant transparent bionanocomposite films for sustainable packaging applications. Carbohydr. Polymers 211, 181–194.
Yang, Z.X., Sun, J.Y., Ran, G.M., He, X.T., 2017. A new solution to Főppl-Hencky membrane equation. J. Mech. 33, N7–N11.
Ye, Y., Liu, Y., Althobaiti, A., Xie, Y.-X., 2019. Localized bulging in an inflated bilayer tube of arbitrary thickness: Effects of the stiffness ratio and constitutive model. Int. J. Solids Struct. 176, 173–184.